

A Collaborative Model-driven Network for MRI Reconstruction

Xiaoyu Qiao^a, Weisheng Li^{a,b,*}, Guofen Wan^c, Yuping Huang^a

^a*Chongqing Key Laboratory of Image Cognition, Chongqing University of Posts and Telecommunications, Chongqing, China*

^b*Key Laboratory of Cyberspace Big Data Intelligent Security, Chongqing University of Posts and Telecommunications, Ministry of Education, Chongqing, China*

^c*College of Computer and Information Science, Chongqing Normal University, Chongqing, China*

Abstract

Deep learning (DL)-based methods offer a promising solution to reduce the prolonged scanning time in magnetic resonance imaging (MRI). While model-driven DL methods have demonstrated convincing results by incorporating prior knowledge into deep networks, further exploration is needed to optimize the integration of diverse priors. Existing model-driven networks typically utilize linearly stacked unrolled cascades to mimic iterative solution steps in optimization algorithms. However, this approach needs to find a balance between different prior-based regularizers during training, resulting in slower convergence and suboptimal reconstructions. To overcome the limitations, we propose a collaborative model-driven network to maximally exploit the complementarity of different regularizers. We design attention modules to learn both the relative confidence (RC) and overall confidence (OC) for the intermediate reconstructions (IRs) generated by different prior-based subnetworks. RC assigns more weight to the areas of expertise of the subnetworks, enabling precise element-wise collaboration. We design correction modules to tackle bottleneck scenarios where both subnetworks exhibit low accuracy, and they further optimize the IRs based on OC maps. IRs across various stages are concatenated and fed to the attention modules to build robust and

*Corresponding author

Email addresses: d210201019@stu.cqupt.edu.cn (Xiaoyu Qiao), liws@cqupt.edu.cn (Weisheng Li), 756281922@qq.com (Guofen Wan), s180231053@stu.cqupt.edu.cn (Yuping Huang)

accurate confidence maps. Experimental results on multiple datasets showed significant improvements in the final results without additional computational costs. Moreover, the proposed model-driven network design strategy can be conveniently applied to various model-driven methods to improve their performance.

Keywords: MRI reconstruction, model-driven, attention mechanism, sparsity, low-rankness

1. Introduction

Magnetic resonance imaging (MRI) is an irreplaceable imaging modality widely employed in clinical scenarios. However, the acquisition of full-sampled raw k-space data is inherently time-consuming, which aggravates patient discomfort and produces artifacts on MR images, limiting the development and application of MR imaging [1].

To address the problem, sub-Nyquist sampling rates are routinely adopted to reduce scanning time, and techniques including parallel imaging (PI) [2] and compressed sensing (CS) [3, 4] enable the reconstruction of MR images from undersampled data. The PI methods [5, 6] exploit the redundancy among k-space data, but the image quality deteriorates at high acceleration factors. In CS-MRI [7, 8], prior knowledge such as sparsity of the k-space data in transform domains is typically exploited to narrow the solution space. Iterative optimization algorithms are then designed to approach the target MR images. However, CS-based methods still face limitations such as reliance on hand-crafted tuning and prolonged iteration processes. [9, 10].

With the notable advancements achieved by deep learning (DL) methods in computer vision tasks, DL-based methods have been successfully introduced into the MRI reconstruction field, which can be broadly categorized into data-driven and model-driven methods [11]. The end-to-end data-driven methods [12, 13, 14, 15, 16, 17, 18] use deep networks to build a pipeline between the inputs (undersampled k-space data or aliased images) and outputs (fully sampled data or artifact-free images), which require a large amount of training data. Another broad family of data-driven methods focuses on distribution learning. Diffusion models including denoising diffusion probabilistic models (DDPM) and score matching with Langevin dynamics (SMLD) have demonstrated convincing results in accelerated MRI. However, the reverse process in diffusion models is time-consuming and not reliable enough

for medical imaging purposes.

In comparison, model-driven methods [19, 20, 21, 22, 23, 24, 25, 26, 27, 28, 29, 30, 31] can be viewed as combinations of conventional and data-driven methods. Prior knowledge is integrated into model-driven networks, whereas deep networks can learn more complex feature representations through learning processes. More specifically, the solution steps of conventional algorithms are unrolled into deep networks. For example, Zhang [20] *et al.* proposed ISTA-Net that unfolds the update steps of ISTA [32] into a deep network. The sparsity transform and its inverse version in ISTA were learned in the network, and a loss function was designed to fulfil the symmetry constraint. Duan [21] *et al.* developed a variable-splitting method to solve the objective function and incorporated the corresponding three-step update process into the network. Sriram [22] *et al.* extended the Variational Network [23] and fulfilled the update steps in k-space by learning end-to-end. Yiasemis [24] *et al.* employed Convolutional Recurrent Neural Networks (CRNNs) within an unrolled network to address the inverse problem. In [33], the optimization process was established using half-quadratic variable splitting method, and a dilated-convolution model was employed to the predict Lagrange multipliers.

In addition to sparsity [34], low rankness is being increasingly applied in inverse problems [35, 36, 37, 38, 39, 40, 41, 42, 43, 44]. For example, Ke [38] *et al.* leveraged low-rank priors to improve sparsity-driven DL-based reconstruction methods. By considering the temporal frames in dynamic MRI as columns of a spatiotemporal matrix, low-rank properties can be utilized. For static MRI reconstruction, low-rank Hankel matrix (LRHM) [45] and LRHM factorization (LRHMF) methods were routinely used [46]. For example, Zhang [39] *et al.* proposed the exploration of simultaneous two-directional low-rankness (STDLR) in k-space data and used an SVD-free algorithm [47] to reduce computation time. Then, alternating direction method of multipliers (ADMM)-based [48] methods were used to minimize the objective function. Some methods use structured low-rank (SLR)[40, 41] algorithms to reduce the computational complexity in completing the Hankel matrix. For example, Pramanik [42] *et al.* proposed a general SLR-based network that significantly reduced the computational complexity. Zhang [43] *et al.* constrained the low rankness of rows and columns of k-space data to reduce computational complexity, and they alleviated the reconstruction errors by introducing prior information. Wang [44] *et al.* split a 2D reconstruction problem into several 1D reconstructions and constructed cascaded Hankel matrices on 1D hybrid data.

A common way to optimize model-driven methods is to incorporate different prior-based regularizers into the objective functions to narrow the solution space more precisely and better avoid falling into local minima. For example, some methods [49, 50, 51, 52] simultaneously incorporated prior knowledge, such as sparsity and low rankness, in dynamic MRI considering the image characteristics. In DL-based reconstruction methods [38, 44], objective functions incorporating sparsity- and low-rankness-based regularizers were used to build a network based on a corresponding iterative algorithm. In addition to explicit prior knowledge, some methods also proposed to impose constraints from learned sensitivity maps for accurate reconstructions [28, 53]. To unroll the optimization steps of a multi-prior-based problem into model-driven networks, unrolled blocks are linearly stacked to alternately introduce constraints from different priors. However, the network needs to find a balance between different prior-based regularizers, leading to slower convergence and consequently suboptimal outcomes. From a more microscopic perspective, different regularization-based blocks specialize in different positions of the target images, resulting in varying speeds to approach the target values for each pixel. Ideally, selecting the most accurate reconstructed results in an element-wise manner in each cascade can effectively accelerate network convergence. This, in turn, allows for more precise intermediate results to be fed into subsequent cascades, increasing the likelihood of approaching the target images with more accurate inputs for the following cascades.

To this end, we propose a versatile collaborative network that different branches based on different priors can simultaneously contribute to the training process to achieve better results. The proposed network is called a collaborative model-driven network (CMD-Net). Our objective is to find the areas of expertise of the subnetworks based on different priors to produce more accurate results for each pixel and seek better convergence. We design three modules in each unrolled cascade within the network: model-driven subnetworks (MNs), attention modules (AMs), and correction modules (CMs). In the proposed network, MNs based on sparsity and low-rankness produce intermediate reconstructions (IRs) in each cascade. With different prior knowledge, the IRs show varying performance in different positions. To fully exploit them, we design an AM to learn the relative confidence (RC) and overall confidence (OC) for these IRs. IRs across various stages are concatenated and fed to the AMs to build robust and precise mappings to the confidence maps. The IRs are fused with the RC maps, which assign more weights to the areas of expertise of the corresponding subnetworks in an element-wise

manner. Considering that when both subnetworks exhibit low accuracy in specific locations, the weighting process cannot effectively improve the results, we further propose a CM. Unlike the subnetworks, the mapping in CMs is directly learned from data without incorporating explicit priors, providing considerable flexibility to compensate for errors brought by the IRs. When the IRs have sufficient high OC values, which means there is high confidence in accepting the RC-fused IRs as the final ones, the correction modules will operate within a relatively small correction range. Otherwise, more weights are assigned to the correction results to further optimize the fused IRs. Data consistency (DC) blocks in CMs were used to maintain consistency with the known sampling data. The optimized IRs from each cascade are used to replace the inputs of the next cascade to accelerate network convergence. Moreover, the results from each cascade are directly fed into the loss function to constrain their functions, and inaccurate confidence maps will result in higher losses. We adopt floating-point operations (FLOPs) to compare the computational costs of different networks. The experimental results show that the proposed method clearly outperforms the networks that linearly stack unrolled cascades. Compared with the state-of-the-art methods on multiple datasets, our method also yields better results. Furthermore, the proposed method is compatible to optimize the existing model-driven networks based on single- or multi-prior. The experimental results show that using the proposed strategy, the performance of different model-driven networks can be improved without increasing computational costs.

The contributions of this study are summarized as follows:

1. We propose a novel collaborative model-driven network design strategy for MRI reconstruction, and the proposed attention-based fusion modules and correction modules in each cascade can effectively maximize the contributions of different prior knowledge based subnetworks to achieve fast and robust convergence.
2. Experimental results on multiple datasets with different acceleration rates, sampling masks, and anatomical structures indicate that the proposed method can achieve better results without extra computational costs.
3. The proposed network design strategy can enhance the performance of other model-driven networks, making it a versatile approach for optimizing both single- and multi-prior based networks.

2. Problem Formulation

In this study, we focused on reconstruction under the PI scenario. The undersampled k -space measurement $y \in \mathbb{C}^{NC}$ is represented by

$$y = \mathcal{A}x + b \quad (1)$$

where $x \in \mathbb{C}^N$ is the unknown MR image to be reconstructed and b is the measurement noise. Here, $N = H \times W$, where H and W are the length and width of y , respectively, and C is the coil number. $\mathcal{A}(\cdot)$ denotes the sampling matrix that is

$$\mathcal{A}(\cdot) = \mathcal{P} \circ \mathcal{F} \circ \mathcal{E}(\cdot) \quad (2)$$

for PI. Here, $\mathcal{P}(\cdot)$ denotes the undersampling matrix, $\mathcal{F}(\cdot)$ denotes the Fourier transform, $\mathcal{E}(\cdot)$ is the expanding operator [22, 24] given as

$$\mathcal{E}(x) = \{\mathcal{S}_1x, \mathcal{S}_2x, \dots, \mathcal{S}_Cx\}, i = 1, 2, \dots, C \quad (3)$$

that applies sensitivity maps to x to generate coil-specific images. \mathcal{S}_i denotes the sensitivity matrix of the i th coil. In contrast, the reduced operator is given by

$$\mathcal{R}\{x_1, x_2, \dots, x_C\} = \sum_{i=1}^C \mathcal{S}_i \otimes x_i, i = 1, 2, \dots, C \quad (4)$$

that integrates the coil images into one image. Hence, the Hermitian transposition of $\mathcal{A}(\cdot)$ is given by:

$$\mathcal{A}^*(\cdot) = \mathcal{R} \circ \mathcal{F}^{-1} \circ \mathcal{P}(\cdot) \quad (5)$$

To reconstruct the MR images from measurement y , the objective function is given as

$$\hat{x} = \arg \min_x \sum_{i=1}^C \|\mathcal{P}\mathcal{F}\mathcal{S}_ix - y\|_2^2 + \lambda \mathcal{U}(x) \quad (6)$$

where the first polynomial is a data fidelity term and the second term denotes different regularizers that incorporate prior information to narrow the solution space. λ was used as a regularization parameter to determine the balance. For example, we express (6) as follows:

$$\hat{x} = \arg \min_x \sum_{i=1}^C \|\mathcal{P}\mathcal{F}\mathcal{S}_ix - y\|_2^2 + \lambda_1 \|\Phi(x)\|_1 \quad (7)$$

in sparsity-based algorithms. Φ is an appropriate transformation field for ensuring the sparsity of the raw data. We adopted an ISTA-based backbone [20] to solve (7), which iterates between the following two steps:

$$r_s^k = x^{k-1} - \alpha^k \mathcal{A}^*(\mathcal{A}(x^{k-1}) - y) \quad (8)$$

$$x_s^k = \tilde{\mathcal{F}}(\text{soft}(\mathcal{F}(r_s^k), \lambda_1)) \quad (9)$$

where k denotes the k th iteration, α^k is the step size, $\mathcal{F}(\cdot)$ is a learned transformation field to ensure improved sparsity, $\tilde{\mathcal{F}}(\cdot)$ is its inverse operator constrained by a customized loss function, and λ_1 is the shrinkage threshold.

For a low-rankness-based method, (6) can be expressed as

$$\hat{x} = \arg \min_x \sum_{i=1}^L \|\mathcal{P}\mathcal{F}\mathcal{S}_i x - y\|_2^2 + \lambda_2 \|\tau(x)\|_* \quad (10)$$

where $\tau(\cdot)$ is the lifting operator used to construct hankel matrices. $\tau(x)$ is a block hankel matrix with dimensions $Cp_1p_2 \times ((H - p_1 + 1)(W - p_2 + 1))$, where p_1 and p_2 are pencil parameters. Singular value decomposition is routinely used to solve nuclear norms; however, it is computationally intensive and time-consuming. As an alternative, some studies leveraged the matrix factorization technique [43]. Some researchers have adopted the iterative reweighted least-squares scheme [54, 44, 42] to majorize the nuclear norm, which can be expressed as

$$\|\tau(x)\|_* \leq \|\tau(x)Q\|_F^2 \quad (11)$$

where Q is the null space of $\tau(x)$ given by

$$Q = [(\tau(x))^H(\tau(x)) + \epsilon I]^{-\frac{1}{4}} \quad (12)$$

$\|\cdot\|_F^2$ denotes the Frobenius norm. We can then solve (10) by alternating between the following two steps.

$$\hat{x}^k = \arg \min_x \sum_{i=1}^C \|\mathcal{P}\mathcal{F}\mathcal{S}_i x^{k-1} - y\|_2^2 + \lambda_2 \|\tau(x^{k-1})Q^{k-1}\|_F^2 \quad (13)$$

$$Q^k = [(\tau(x^{k-1}))^H(\tau(x^{k-1})) + \epsilon I]^{-\frac{1}{4}} \quad (14)$$

we extracted x^k from the lifting operator by leveraging the commutativity of the convolutions [42] as

$$\|\tau(x)Q\|_F^2 = \|\mathcal{D}(Q)x\|_F^2 \quad (15)$$

where $\mathcal{D}(Q)$ is constructed by vertically cascading $\mathcal{D}(q_j)$. q_j is the j -th column of matrix Q and $\mathcal{D}(q_j)$ is a block Hankel matrix constructed from the elements of q_j . Thus, we can rewrite (13) as follows:

$$\hat{x}^k = \arg \min_x \sum_{i=1}^C \|\mathcal{P}\mathcal{F}\mathcal{S}_i x^{k-1} - y\|_2^2 + \lambda_2 \|\mathcal{D}(Q^{k-1})x^{k-1}\|_F^2 \quad (16)$$

Here we solve (16) by iterating the following two steps [55, 56, 44]:

$$r_l^k = \lambda_2 (\mathcal{D}(Q^{k-1}))^H \mathcal{D}(Q^{k-1}) x^{k-1} \quad (17)$$

$$x_l^k = x^{k-1} - \beta^k (\mathcal{A}^*(\mathcal{A}(x^{k-1}) - y) + 2r_l^k) \quad (18)$$

3. Method

3.1. Network Structure

The proposed network structure and its components are illustrated in Fig. 1. Fig. 1 (a) shows the overall network structure. In the network training process, the undersampled k-space data $y \in \mathbb{C}^{NC}$ as well as the corresponding sensitivity maps $\mathcal{S} \in \mathbb{C}^{NC}$ and masks $\mathcal{P} \in \mathbb{R}^N$ are fed to the network. MR images are stored using complex values, and some studies have proposed complex convolutions [13] to achieve better results; however, this is not our focus. Therefore, we leveraged the common method that two channels were used to store the real and imaginary parts in this study, and $y \in \mathbb{C}^{NC}$, $\mathcal{S} \in \mathbb{C}^{NC}$ were transferred to $y \in \mathbb{R}^{2NC}$, $\mathcal{S} \in \mathbb{R}^{2NC}$ before they are fed into the network. Besides, the coil-combined image x^0 is obtained from the zero-filled measurement y and fed to the network. Then, several iteration blocks were stacked to form the main body, and each block is referred to as a cascade. Through stacked cascades, the network finally outputs the reconstructed MR images. Each cascade comprised three parts: MNs (green blocks), AMs (yellow blocks), and CMs (blue blocks). Fig. 1 (b)–(f) present the detailed structures of the modules, which are introduced in the following subsections.

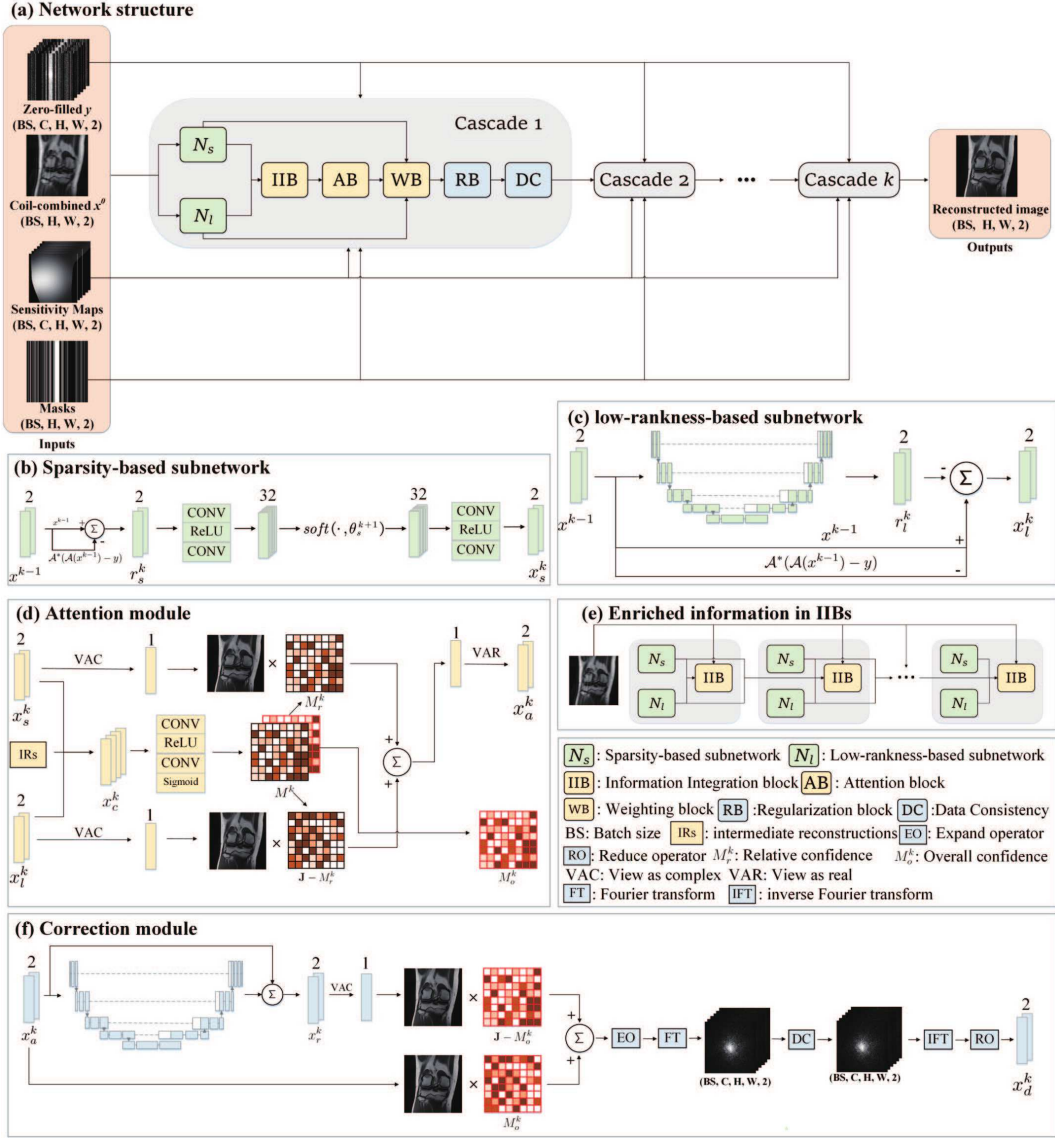


Figure 1: (a): the structure of the proposed network. (b): the structure of the sparsity based sub-network (N_s in (a)). (c): the structure of the low-rank based sub-network (N_l in (a)). (d): the structure of the attention modules (the yellow blocks in (a)), each of which include an information integration block (IIB), an attention block (AB), and a weighting block (WB). (e): the enriched information in IIBs. (f) the structure of the correction modules (the blue blocks in (a)), each of which includes a regularization block (RB) and a data consistency (DC) block.

3.2. Model-driven Subnetworks

In this study, we proposed the precise integration of different types of prior knowledge into the network to achieve better performance. We planned to choose prior knowledge commonly used in accelerated MRI to ensure the versatility and effectiveness of the network. Moreover, there should be better complementarity between different types of prior knowledge than the same knowledge, which can be exploited. Therefore, we designed a sparsity-based subnetwork (N_s in Fig. 1 (a)) and low-rankness-based subnetwork (N_l in Fig. 1 (a)). For N_s , we adopted the sparsity-based ISTA-Net [20] as the backbone network. The learned $\mathcal{F}(\cdot)$ and $\tilde{\mathcal{F}}(\cdot)$ are implemented using cascaded convolutional layers and ReLU activation functions, as shown in Fig. 1 (b). We remarked the output of N_s in the k th iteration as x_s^k , and we have

$$x_s^k = N_s(x^{k-1}) \quad (19)$$

and N_s denotes the iterative processes in (8) and (9).

N_l in each cascade is constructed by unrolling (17) and (18) into the network. For (17), essentially $(\mathcal{D}(Q))^H \mathcal{D}(Q)x$ can be regarded as a projection acting on x , which is determined by Q , and Q at each iteration will also be updated according to the status of x . Therefore, we relaxed the constraint on (17) and used U-Net to learn the mapping directly, as shown in Fig. 1 (c). Although the constraint from the prior knowledge is relaxed, we can still exploit the complementary information from different subnetworks. Besides, the subnetwork gains enhanced flexibility to learn appropriate features from the data to deal with different input scenarios and improve its performance.

We used N_{lu} to represent U-Net, and thus, we have

$$r_l^k = \lambda_2 N_{lu}(x^{k-1}) \quad (20)$$

Similar to (19), we obtained

$$x_l^k = N_l(x^{k-1}) \quad (21)$$

where N_l denotes the processes in (20) and (18), respectively.

3.3. Attention Modules

The AMs include the yellow blocks in Fig. 1; the details are shown in Fig. 1 (d). The first objective of an AM is to maximize the contributions of subnetworks in their respective areas of expertise. To achieve this, we

design the RC maps to precisely weight the IRs produced by subnetworks in an element-wise manner. The RC essentially indicates the confidence level to accept the pixel values as the final predictions. Consequently, when the predicted value from one subnetwork matches the target closer than the other one, the RC value should be closer to one, signifying high confidence. We used M_r^k to represent the RC map in the k -th cascade, and during the weighting process, we transferred x_s^k and x_l^k back to complex values (i.e., $x_s^k, x_l^k \in \mathbb{R}^{2N} \rightarrow x_s^k, x_l^k \in \mathbb{C}^N$) and then created a Hadamard product between M_r^k and x_s^k . x_l^k is similarly multiplied by $\mathbf{J} - M_r^k$. We used N_a to represent the weighting block (WB), and the weighted output is given by

$$x_a^k = N_a(x_s^k, x_l^k) = x_s^k \odot M_r^k + x_l^k \odot (\mathbf{J} - M_r^k) \quad (22)$$

where x_s^k and x_l^k are IRs produced by subnetworks in the k -th cascade, x_a^k is the RC-weighted result and $\mathbf{J} \in \mathbb{R}^N$ is a matrix filled with one.

However, there remains a flaw that hinders the proposed method from producing accurate results even with ideal (i.e., accurate) RC maps. In situations where the predicted values of a pixel from both subnetworks are simultaneously bigger or smaller than the target values, the RC-based weighting process fails to obtain more precise values, resulting in suboptimal convergence speed. In other words, even with ideal RC maps, the confidence level to accept x_a^k as the final prediction is compromised in these pixels. To address the issue, we introduce OC maps, which learn the confidence of x_a^k , while CMs are designed to further optimize the low-OC areas. Consequently, the AMs are designed to simultaneously learn the RC and OC of the IRs in different cascades.

Empirically, learning from the richer features in subnetworks could improve the accuracy of RC and OC maps. However, this approach may introduce higher computational costs and potentially limit the versatility of the network. Therefore, we proposed the design of an information integration block (IIB) to learn the confidence maps from IRs across various subnetworks and cascades. By incorporating richer information from IR value maps across various stages, we can establish a more robust mapping to the target confidence maps, thereby enhancing the overall effectiveness of the network. The IIB in the k -th cascade is given as:

$$x_c^k = \begin{cases} \mathcal{C}[x^0, x_s^k, x_l^k], & k = 1 \\ \mathcal{C}[x^0, x_s^{k-1}, x_l^{k-1}, x_s^k, x_l^k], & k > 1 \end{cases} \quad (23)$$

where x_c^k is the input of the attention blocks (ABs) and $\mathcal{C}[\cdot]$ denotes a concatenation operator on the channel dimension. Therefore, the input for the ABs consists of the coil-combined measurements x^0 and the IRs from the current and the previous cascade (if they exist). This is aimed to incorporate short and long-range information of the pixel values to build a stable mapping. It is worth emphasizing that the design of the input features is highly flexible, based on the fundamental concept that richer inputs generally yield more robust confidence maps. This will be further discussed in Section 4.3.

Then, x_c^k is fed into an AB comprising two convolutional layers, each of which connects to an activation layer. Here we chose the ReLU and sigmoid functions, respectively. After the four-layer attention block, we obtained a two-channel attention map M^k , given as:

$$M^k = \mathcal{C}[M_r^k, M_o^k] = N_{AB}(x_c^k) \quad (24)$$

where N_{AB} denotes the ABs. Each element in M^k lies between zero and one. We separated M^k into M_r^k and M_o^k , where M_o^k is the OC maps. The OC maps as well as the weighted IRs (*i.e.*, x_a^k) are fed to the correction modules.

3.4. Correction Modules

Through AMs, the pixels reconstructed by proper subnetworks can have larger weights, and the gap between intermediate outputs and targets can be narrowed. However, there may be instances where the intermediate values from both subnetworks are significantly bigger or smaller than the target values. In such cases, the RC-based weighting process encounters challenges in bringing the intermediate reconstructions closer to the target, leading to suboptimal convergence. Therefore, we proposed a correction module to further improve the network performance, especially on these pixels. Each correction module consists of a regularizer block (RB) and a data consistency (DC) block. The RB block is given as:

$$x_r^k = x_a^k + N_r(x_a^k) \quad (25)$$

where N_r is implemented by a U-Net backbone. We design a residual structure to make N_r directly learn the updated information. Unlike subnetworks, conventional prior knowledge is not explicitly or implicitly involved in narrowing the solution space, that RBs directly learn the mapping from data. When the outputs from AMs are of sufficient accuracy for some pixels, replacing them with the RB results could potentially introduce new errors.

Therefore, we adopted the OC maps produced in AMs, which represent the confidence to accept the AM-based IRs as the final results in a element-wise manner. The OC-based correction process is given as:

$$\begin{aligned} x_o^k &= x_a^k \odot M_o^k + x_r^k \odot (\mathbf{J} - M_o^k) \\ &= x_a^k \odot M_o^k + (x_a^k + N_r(x_a^k)) \odot (\mathbf{J} - M_o^k) \end{aligned} \quad (26)$$

where x_o^k is the OC-weighted output.

Finally, we placed a data consistency (DC) block to keep consistency with the known sampling data. The DC block is widely used in MR reconstruction models to maximize the use of sampled data to revise the reconstructed results, which is given as

$$y_d^k = \begin{cases} y_o^k, & y_o^k \notin \Omega \\ \frac{y_o^k + \mu y}{1 + \mu}, & y_o^k \in \Omega \end{cases} \quad (27)$$

where y_d^k is the output of the DC blocks, y_o^k is the multi-coil k-space data of x_o^k and Ω is a subset of fully-sampled k-space data, representing sampled data points. For the sampled point, a learned μ is used to adjust its ratio with the measurement y . Finally, y_d^k is transferred back to the image domain using inverse Fourier transform (IFT) and the reduce operator, and the optimized x_d^k , instead of x_s^k and x_l^k , is fed into the $(k + 1)$ th N_s and N_l blocks. Our approach enhances the reconstruction results in each cascade, enabling the subsequent cascade to have a better chance of approaching the target images, thus improving the overall network performance. We used N_c to represent the processes in (26) and (27) and obtained $x_d^k = N_c(x_a^k)$. Here, x_d^k is equal to x^{k+1} , and is fed into the next cascade. Finally, we have:

$$\begin{aligned} x^k &= x_d^k = N_c(x_a^k) = N_c(N_a(x_s^k, x_l^k)) \\ &= N_c(N_a(N_s(x^{k-1}), N_l(x^{k-1}))) \end{aligned} \quad (28)$$

3.5. Settings and Loss Function

We set the cascade number to 10 in the network. α^k , β^k , λ_1 , λ_2 were directly learned in the network. For N_s , the number of channels in the convolutional layers was set to 32, 32 in $\mathcal{F}(\cdot)$, and 32, 2 in $\tilde{\mathcal{F}}(\cdot)$. The kernel size in the convolutional layers was set to three and the padding size was set to one. For U-Net in N_l , the number of pooling layers was set to four and the number of channels was set to 16, 32, 64, and 128. For the convolutional

layers in AMs, the number of channels was set to 32 and 2. The kernel size in the convolutional layers was set to 3 and the padding size was set to 1. For U-Net in the correction modules, the number of pooling layers was set to 4, and the number of channels was set to 4, 8, 16, and 32.

The experiments were conducted on a RTX 3090 GPU. During training, the batch size was set to 1, and the learning rate was set to 1e-3. The mean squared error (MSE) was adopted to train the network, expressed as

$$\mathcal{L}_{MSE}(x_g, \hat{x}) = \|x_g - \hat{x}\|_2^2 \quad (29)$$

where x_g is the target image (ground truth) and \hat{x} is the predicted image. The final output of the network and the intermediate outputs from each cascade are fed to the loss function to supervise the corresponding modules:

$$\mathcal{L} = \sum_{k=1}^K [\gamma_1^k \mathcal{L}_{MSE}(x_g, x_d^k) + \gamma_2 \|\tilde{\mathcal{F}}(\mathcal{F}(r_s^k)) - r_s^k\|_2^2], \gamma_1^i = 10^{\frac{k-K}{K-1}} \quad (30)$$

where K is the total number of stacked cascades. In this study, $\{\gamma_1^i\}_{k=1}^K$ is an increasing sequence to assign different weights to the outputs from different cascades [33], and γ_2 , which was used to fulfil the symmetry constraint, was set to 0.01.

4. Experimental Results

In this section, we compared the reconstruction performance of the proposed CMD-Net with state-of-the-art methods on various datasets to demonstrate its superiority. Ablation studies were conducted to demonstrate the necessity of the proposed modules. Furthermore, we extended the collaboration strategy to other model-driven methods, illustrating its versatility as an enhancement strategy.

4.1. datasets

In this study, we utilized three datasets to evaluate our methods. The first dataset is a publicly available knee dataset [42, 23, 21] comprises five sequences: coronal proton density (PD), coronal fat-saturated PD (PDFS), axial fat-saturated T2, Sagittal fat-saturated T2 and Sagittal PD. Each sequence included MR images from 20 patients, with each sequence consisting of approximately 40 slices. In this study, the ratio of the training, validation,

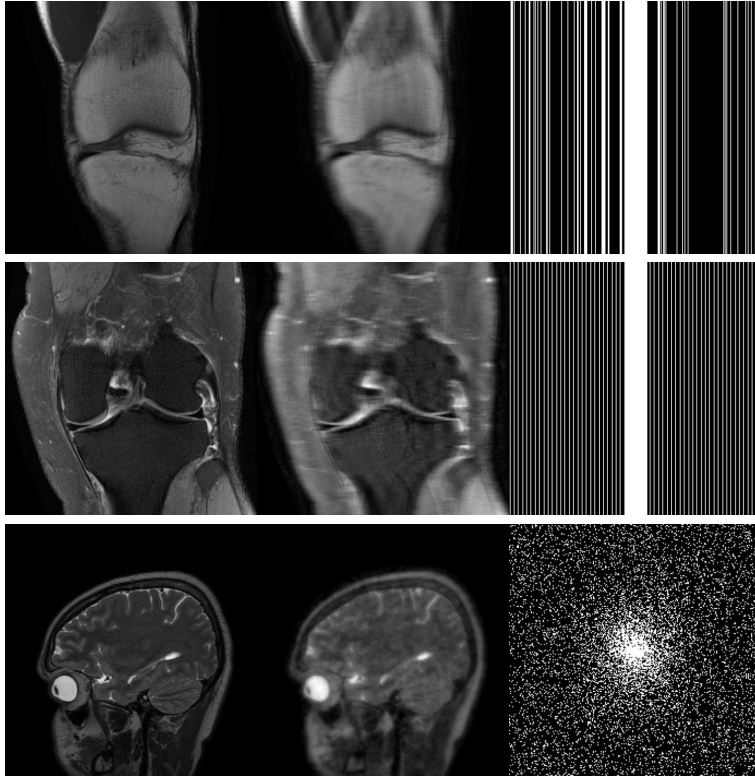


Figure 2: examples of training data in the knee dataset (the first row), fastMRI dataset (the second row) and the brain dataset (the third row). The first column displays the ground truth images, the second row shows the zero-filled images and the third row are the corresponding sampling masks.

and testing data was set to 6:2:2. None of the validation or testing data was used for training, and vice versa. The best-performing networks on the validation sets were selected and preserved for testing and comparison of their results.

We also conducted our experiments on the fastMRI dataset [57]. Given the limitations of our training hardware, we trained the networks on a subset of the fastMRI knee dataset. Specifically, 1199 slices were used to train the networks with the image size of 640×368 . Because the fastMRI dataset did not provide fully sampled test data, we partitioned the validation set into a test set and a new validation set. During training, 100 slices were used for validation. Finally, 950 slices were used to evaluate the network performance. All the data were randomly selected, ensuring no overlap among them.

In addition to these two knee datasets, we incorporated a brain dataset [27] to further strengthen our findings. This dataset contains 360 slices for training and 164 slices for testing. We randomly selected 10 slices from the test set for validation, leaving 154 slices for evaluating the network performance.

For the knee dataset and fastMRI dataset, we applied random and equispaced Cartesian undersampling with 4-fold and 6-fold acceleration to the k-space data, respectively, sampling 24 lines at the central region. For the first knee datasets, the coil sensitivity maps were pre-computed using ESPIRiT [58], and these sensitivity maps are provided in the dataset. For fastMRI dataset, we pre-computed the corresponding sensitivity maps using the Sippy [59] toolbox. For the brain dataset, coil sensitivity maps and 2D random sampling masks are also included in the dataset. Samples of MR images and the corresponding sampling masks are shown in Fig. 2. More detailed data collection parameters of the aforementioned dataset are available in the corresponding papers [23, 57, 27].

4.2. Comparison with cutting-edge methods

We compared the performance of our network with some representative methods. Experimental results conducted on the coronal PD and PDFS sequences, as well as the fastMRI dataset, are presented in Table 1. We tested $4\times$ and $6\times$ accelerations, which means that we sampled a quarter and a sixth of the raw data as the network inputs, respectively. We used the most commonly used PSNR and SSIM metrics to evaluate the performance of different networks. In the table, the zero-filled method denotes the baseline results, where the undersampled raw data are filled with zeros. TV denotes the conventional total variation algorithm [60]. U-Net denotes the basic U-Net structure [57]. The number of pooling layers was set to 4, and the number of corresponding channels were set to 32, 64, 128, and 256. D5C5 [61], ISTA-Net [20], VS-Net [21], E2E-VarNet [22], ReVarNet [24] and vsharp [33] are model-driven networks proposed in recent years. Considering that the computational costs of different networks varied significantly, which subsequently affects the reconstruction results, we simultaneously compared the FLOPs of different networks for a fair comparison. The FLOPs of different networks evaluated on the coronal PD sequence are shown in Table 2. For ReVarNet, it cannot be directly trained on our GPU (24GB). Considering the number of cascade is significant for achieving superior reconstruction performance, we preserved 15 cascades in the network and reduced the number

Table 1: The quantitative results on coronal PD, coronal PDFS sequences and the Fastmri dataset compared with the state-of-the-art methods.

Sequence	Method	PSNR		SSIM	
		4×	6×	4×	6×
Coronal PD	zero-filled	31.3089±3.3939	30.5176±3.3902	0.8778±0.0713	0.8626±0.0799
	TV	33.7498±3.1753	32.3290±3.2159	0.8851±0.0657	0.8658±0.0725
	U-Net	36.8984±2.7072	34.7352±2.7863	0.9361±0.0610	0.9133±0.0682
	D5C5	38.7903±2.8408	35.9697±2.7990	0.9509±0.0587	0.9259±0.0689
	ISTA-Net	39.2910±2.8423	35.5220±3.0915	0.9471±0.0567	0.9138±0.0717
	VS-Net	40.1649±2.8767	37.0604±2.7927	0.9591±0.0569	0.9358±0.0648
	E2E-VarNet	39.3592±2.9368	36.8949±3.3872	0.9542±0.0662	0.9342±0.0775
	ReVarNet	40.2545±2.8766	37.3683±2.7869	0.9590±0.0588	0.9379±0.0677
	vSharp	39.6096±2.8842	37.2795±2.5143	0.9472±0.0614	0.9048±0.0629
	CMD-Net (ours)	41.0221±3.0523	38.1785±2.9848	0.9634±0.0610	0.9441±0.0727
Coronal PDFS	zero-filled	32.0299±2.0273	31.2221±2.0575	0.7964±0.0998	0.7587±0.1172
	TV	33.7256±1.9058	32.7328±1.8850	0.8124±0.0752	0.7920±0.0796
	U-Net	34.4367±0.6572	33.2028±2.5662	0.8183±0.0106	0.7758±0.1222
	D5C5	34.9671±2.8261	33.4189±2.4765	0.8250±0.1106	0.7854±0.1223
	ISTA-Net	34.4990±2.6389	33.4569±2.5758	0.8198±0.1066	0.7854±0.1214
	VS-Net	34.6847±2.7134	33.5010±2.6100	0.8259±0.1073	0.7842±0.1229
	E2E-VarNet	34.6274±2.7331	33.1626±2.4742	0.8234±0.1101	0.7804±0.1244
	ReVarNet	34.8522±2.7461	33.3146±2.5604	0.8272±0.1080	0.7832±0.1232
	vSharp	35.1235±2.4473	33.6029±2.2205	0.8194±0.0841	0.7924±0.1075
	CMD-Net (ours)	35.6824±3.0160	34.2930±2.8255	0.8401±0.1071	0.8041±0.1273
FastMRI	zero-filled	32.8883±3.0920	32.0634±3.0960	0.8856±0.0681	0.8679±0.0758
	TV	35.3960±2.8296	33.6309±2.7932	0.8920±0.0610	0.8696±0.0704
	U-Net	36.5615±3.0155	35.2409±2.9859	0.9188±0.0622	0.8959±0.0694
	D5C5	37.4408±3.3691	35.6572±3.0195	0.9297±0.0638	0.9056±0.0712
	ISTA-Net	36.8610±3.3105	34.9415±3.2019	0.9260±0.0655	0.8917±0.0698
	VS-Net	37.6398±3.4316	35.0945±3.1050	0.9284±0.0629	0.8953±0.0713
	E2E-VarNet	38.8871±3.5091	36.5089±2.9326	0.9359±0.0628	0.9131±0.0702
	ReVarNet	38.6352±3.1220	37.0392±2.8924	0.9242±0.0624	0.9126±0.0626
	vSharp	38.9048±3.4802	36.6015±2.9659	0.9258±0.0642	0.9025±0.0661
	CMD-Net (ours)	39.4191±3.7731	37.3497±3.1327	0.9395±0.0622	0.9195±0.0686

Table 2: FLOPs of different model-driven networks on coronal PD sequence.

Networks	FLOPs(G)
D5C5	186.55
ISTA-Net	120.13
VS-Net	265.89
E2E-VarNet	187.39
ReVarNet	204.87
vSharp	609.63
CMD-Net (ours)	208.93

of channels in ReVarNet from 64 to 32 to reduce its FLOPs to the same level as in our model. Considering that D5C5 had lower FLOPs, we increased the number of cascades from five to seven in the experiments to improve its performance. For the other networks, we tried our best to preserve the net-

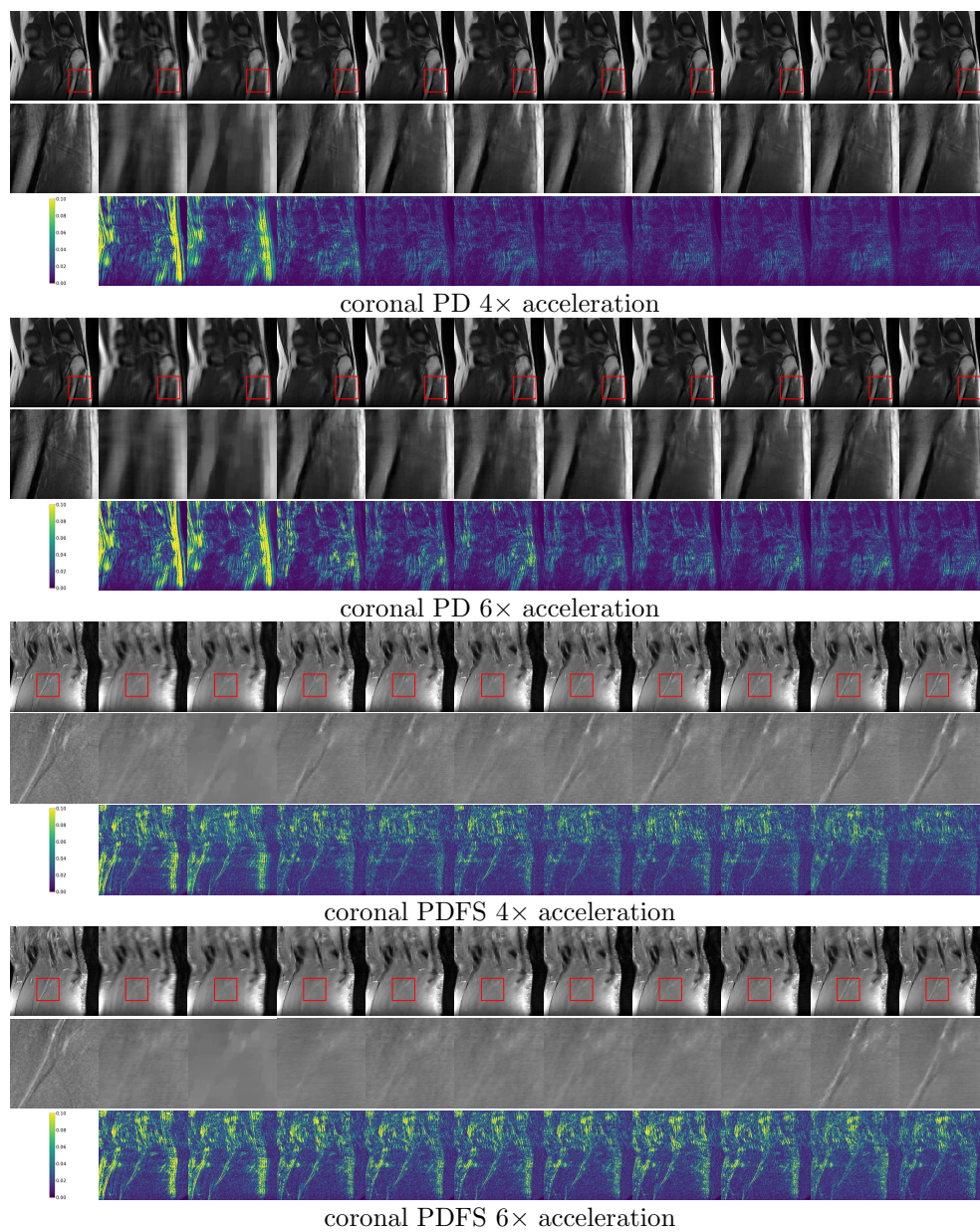


Figure 3: Examples of reconstructed images of different methods. The first rows are the reconstructed images of different methods, the second rows are the zoomed details in the red boxes and the third rows are the corresponding error maps.

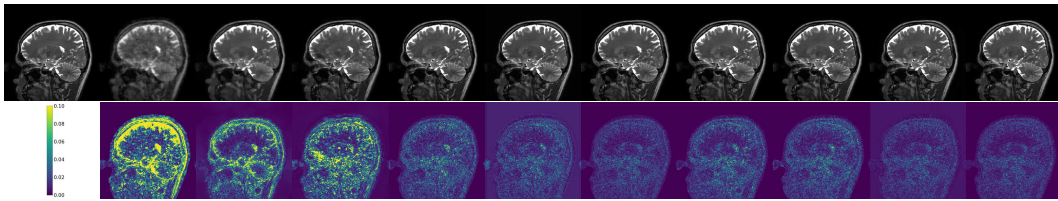


Figure 4: Examples of reconstructed brain MR images and the corresponding error maps.

work parameters in their published papers. As shown in the table, ISTA-Net exhibits relatively lower FLOPs compared to other networks. However, we did not observe significant improvements in the results when increasing its parameters. Hence, we retained the announced hyper-parameters, as in their study. The results shown in the tables demonstrate that the proposed CMD-Net can achieve the best performance among the chosen methods without additional computational cost.

Examples of the reconstructed images from different methods are plotted in Fig. 3. Here, we presented the results obtained from the coronal PD and PDFS sequences with 4-fold and 6-fold acceleration, while the results on the fastMRI dataset exhibited similar outcomes. The layout of the images is as follows: the first rows display the reconstructed images from various methods, while the second rows display the zoomed details of the images within the red boxes. The third rows show error maps between the reconstructed images and the ground truth images. Figure. 3 clearly demonstrates that our method excels in recovering image details with the fewest errors among all methods.

Besides, examples of reconstructed images as well as the corresponding error maps on the brain MRI data are shown in Fig. 4, and the quantitative results are presented in Table 3. When applied to a smaller dataset with different anatomy and sampling trajectories, not all comparison methods achieve superior results. Conversely, our method consistently proves its superiority, emphasizing its effectiveness.

4.3. Ablation studies

We designed ablation studies to demonstrate the improvements achieved by the proposed modules. The experimental results obtained from the coronal PD sequence are presented in Table 4. Here, we compared the following networks:

Table 3: The quantitative results on the brain MRI dataset compared with the state-of-the-art methods.

Method	PSNR	SSIM
zero-filled	27.8175±0.1860	0.8437±0.0502
TV	31.8378±1.8519	0.8072±0.0731
U-Net	30.8815±2.2455	0.8047±0.1872
D5C5	36.9407±1.4127	0.9627±0.0125
ISTA-Net	36.9413±1.4091	0.8891±0.1192
VS-Net	39.6361±1.2324	0.9770±0.0106
E2E-VarNet	35.2120±4.6142	0.9428±0.0618
ReVarNet	37.5542±1.2790	0.9625±0.0169
vSharp	38.4702±3.3468	0.8602±0.1659
CMD-Net (ours)	40.2080±1.1206	0.9786±0.0125

- addition: The attention-based fusion modules and the correction modules are removed. The mean values of the intermediate results from N_s and N_l are directly fed to the next cascades.
- w/o attention modules: Only the attention-based fusion modules are removed compared with the proposed network. The mean values, instead of the weighted images are fed to the correction modules, and the corrected images in CMs directed replaced the fused images (*i.e.*, without the OC-based weighting process).
- w/o enriched inputs: only the IRs in the current cascade are fed to the AM to learn the confidence maps.
- w/o RC: The AMs only learn the OC maps, and mean values of IRs are fed to the CMs.
- w/o OC: The AMs only learn the RC maps, and the corrected images in CMs directed replaced the weighted images.
- w/o correction: only the correction modules are removed from the proposed network, which means that the weighted IRs from AMs are fed to the next cascades.
- w/o intermediate losses: only the MSE of the final outputs and the ground truth images is incorporated in the loss function. Besides, the ISTA-based losses are still incorporated to constrain the subnetwork function.
- original: The proposed network structure.

Table 4: Results of ablation studies on coronal PD sequence with 4-fold and 6-fold acceleration rates.

Method	PSNR		SSIM		FLOPs(G)
	4×	6×	4×	6×	
addition	36.2822±2.4613	33.8586±2.2615	0.8525±0.0677	0.7781±0.0688	193.05
w/o attention	40.5671±3.0143	37.8001±2.7495	0.9618±0.0614	0.9425±0.0691	201.07
w/o enriched inputs	40.9493±3.0194	38.0659±3.0012	0.9626±0.0604	0.9433±0.0721	205.14
w/o RC	40.8017±2.9238	37.9258±2.8809	0.9617±0.0584	0.9430±0.0685	208.26
w/o OC	40.9416±3.0891	38.1156±2.9722	0.9630±0.0622	0.9438±0.0715	208.26
w/o correction	40.4576±3.0865	37.6690±3.4823	0.9580±0.0642	0.9392±0.0730	200.24
w/o inter losses	40.4352±3.1200	37.6014±3.1824	0.9597±0.0650	0.9414±0.0716	208.93
original	41.0221±3.0523	38.1785±2.9848	0.9634±0.0610	0.9441±0.0727	208.93

Table 5: Reconstruction results with different inputs in the AMs.

inputs	channel	PSNR		SSIM		FLOPs(G)
		4×	6×	4×	6×	
4	32	40.9493±3.0194	38.0659±3.0012	0.9626±0.0604	0.9433±0.0721	205.14
8	32	40.9803±3.0296	38.1735±3.0246	0.9629±0.0610	0.9439±0.0732	207.58
10	32	41.0221±3.0523	38.1785±2.9848	0.9634±0.0610	0.9441±0.0727	208.93
14	32	41.0672±3.0063	38.1687±3.0691	0.9633±0.0610	0.9440±0.0732	211.10
14	64	41.0258±2.9613	38.1636±3.1465	0.9634±0.0610	0.9437±0.0759	221.14
18	32	40.9556±3.0352	38.2047±3.1269	0.9629±0.0606	0.9439±0.0747	213.01
18	64	41.1108±3.0005	38.2279±2.9977	0.9636±0.0600	0.9443±0.0723	224.94

The 'addition' method denotes the simplest parallel network, in which the mean values of the intermediate results from N_s^k and N_l^k are directly fed to the $(k+1)$ th cascade. Compared with the original method, the improvements brought by the proposed modules is notable. When the AMs are removed from the original method, the subnetworks also contribute equally to the IRs. However, because different subnetworks have varying abilities to reconstruct images, this process cannot guarantee improvements in IR results. Furthermore, directly replacing fused IRs with corrected images in CMs without learned OC maps could potentially introduce new errors. As a result, the network ('w/o attention') showed worse performance. We further evaluated the contribution of different components in the attention modules (*i.e.*, 'w/o enriched inputs', 'w/o RC' and 'w/o OC' methods). As shown in the table, deteriorations of varying degrees were observed in the three ablation networks, demonstrating the necessity of the modules. Similarly, removing the CMs from the network limited the network's flexibility, and it could not effectively handle low-OC pixels, resulting in slower convergence and suboptimal results. The intermediate losses imposed on each cascade play a crucial role in constraining the function of the confidence maps, because inaccurate

confidence maps lead to increased losses. When these intermediate losses are removed, only the final output is constrained with MSE loss to guide network training. This results in slower convergence of the network and a deterioration in the performance of the reconstructed images. Furthermore, we observed that the designed modules are easy to apply, resulting in noticeable improvements, while the increment in FLOPs is negligible. Compared with the naive 'addition' methods, the CMD-Net showed an increase in FLOPs of less than 10%, yet achieves great improvements in results, demonstrating its effectiveness.

In addition, we conducted a comparison of network performance using different inputs in the AMs, with results detailed in Table 5. The values in the first column represent the channel number of the input information in AMs. Specifically, the 4-channel input signifies the combination of the IRs in the current cascades, while the 8-channel input represents the combination of IRs in both the current and previous cascades. The remaining methods further include the coil-combined x^0 , and more information from previous cascades. The values in the second column denote the number of channels in the convolutional layers in the ABs. We can observe from the table that richer information generally correlates with better reconstruction performance. However, it's important to note that increasing input richness should be accompanied by a corresponding increase in the number of channels. Mismatched input and network scale may potentially result in inferior outcomes.

4.4. Comparisons with non-parallel network structure

All the ablation studies in Table 4 utilize the proposed parallel network structure, where different subnetworks leverage different prior knowledge and the results from the subnetworks are integrated in different ways. To further illustrate its efficacy compared to a non-parallel structure, we conducted comparisons with two types of networks: (a) where one subnetwork is removed, and (b) where prior knowledge is incorporated into a single objective function. For type (a), the computational costs of these networks are reduced because the components in the other subnetwork, as well as the components used to integrate the subnetworks, are removed. To eliminate the interference caused by varied computational costs, we augmented the parameters of type (a) networks so that they can have similar FLOPs as the proposed network. Additionally, we considered that the network depth (i.e., the number

Table 6: Comparisons with non-parallel networks on coronal PD sequence with 4-fold and 6-fold acceleration rates.

Method	PSNR		SSIM		FLOPs(G)
	4×	6×	4×	6×	
L+cascades	40.2784±2.9231	37.1909±32.8541	0.9558±0.0591	0.9296±0.0684	198.18
L+depth	40.0213±2.9835	37.3131±2.8203	0.9556±0.0600	0.9296±0.0691	193.08
S+cas+depth	38.7506±2.9279	35.9477±2.8162	0.9485±0.0590	0.9234±0.0679	228.93
L+S	39.8596±2.9063	37.5395±2.8677	0.9552±0.0588	0.9359±0.0701	201.07
CMD-Net (ours)	41.0221±3.0523	38.1785±2.9848	0.9634±0.0610	0.9441±0.0727	208.93

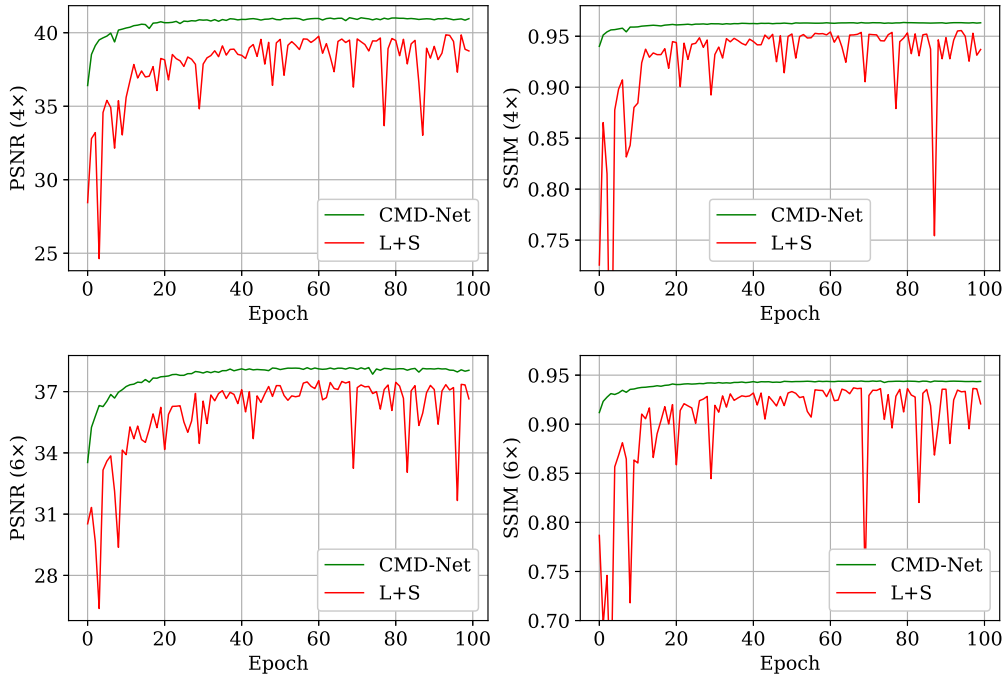


Figure 5: The test PSNR and SSIM results of 'L+S' and the proposed CMD-Net at 4-fold and 6-fold acceleration.

of hidden channels) and the number of cascades are two significant hyper-parameters that affect the reconstruction performance. Therefore, we tested both methods (i.e., adding the number of cascades or channels) to unify the FLOPs of the networks.

The designed networks are listed in Table 6. In these method names, the capital 'L' denotes the network with only the N_l branch and 'S' with the N_s branch. "+cascades" and "+depth" denote the appropriate addition of

the number of channels and cascades in the corresponding networks, respectively. For the L+cascades method, the number of cascades was increased to 16 from 10. For method L+depth, the number of channels in the subnetworks increased from 16 to 20, and from 4 to 8 in the correction modules. For the sparsity based branch, because its FLOPs is relatively lower, merely increasing the cascade or depth makes the network difficult to train. Therefore, we simultaneously augmented the number of channels in the learned sparse transform from 32 to 48 and the number of cascades from 10 to 15. Note that L+S in the table solves the following problem:

$$\hat{x} = \arg \min_x \sum_{i=1}^C \|\mathcal{P}\mathcal{F}\mathcal{S}_i x - y\|_2^2 + \lambda_1 \|\Phi(x)\|_1 + \lambda_2 \|\tau(x)\|_* \quad (31)$$

which is the common method to solve multi-prior-based methods, and the iterative solution steps are given by:

$$\begin{cases} r_l^k = \lambda_2 N_{lu}(x^{k-1}) \\ x_l^k = x^{k-1} - \beta^k (\mathcal{A}^*(\mathcal{A}(x^{k-1}) - y) + 2r_l^k) \\ x^k = \tilde{\mathcal{F}}(\text{soft}(\mathcal{F}(x_l^k), \lambda_1)) \end{cases} \quad (32)$$

Essentially, the output of the low-rank-based branch is fed to the N_s branch in L+S, and different priors contribute to the results in an alternating form. Conversely, the outputs of N_l and N_s are directly fed into the attention modules in our method to optimize the intermediate results in cascades. As shown in the table, our method outperforms the other methods with 4× and 6× accelerations. Besides, we plotted the PSNR and SSIM test results of 'L+S' and our method across epochs, as shown in Fig 5. We observed that the convergence of the proposed CMD-Net is faster and more stable. These experimental results suggest that the proposed parallel network offers a more efficient approach to designing a model-driven network.

4.5. Applying to other methods

Another significant advantage of the proposed method is that the network design strategy can be easily applied to other model-driven methods to improve the results. We conducted experiments using VS-Net and E2EVarNet, and the experimental results are presented in Table 7. Considering that applying the proposed network design to other unrolling methods will inevitably increase the computational costs, we tried two ways to unify the

Table 7: Results of applying our method to other model-driven networks on coronal PD sequence with 4-fold and 6-fold acceleration rates.

Method	PSNR		SSIM		FLOPs(G)
	4×	6×	4×	6×	
VS-Net	40.1649±2.8767	37.0604±2.7927	0.9591±0.0569	0.9358±0.0648	265.89
VS&L	40.7821±4.9701	38.1436±3.4582	0.9602±0.0656	0.9438±0.0707	207.58
VS-Net+	40.4903±2.8800	37.4789±2.7207	0.9608±0.0558	0.9388±0.0651	398.83
VS&L+	40.9462±3.5993	38.0641±5.0574	0.9626±0.0640	0.9436±0.0806	405.64
E2EVarNet	39.3592±2.9368	36.8949±3.3872	0.9542±0.0662	0.9342±0.0775	187.87
E2EVarNet&L	41.0484±3.0959	38.2754±3.0162	0.9638±0.0592	0.9450±0.0718	205.35
E2EVarNet+	38.9097±3.4703	36.0596±2.9721	0.9511±0.0785	0.9273±0.0740	326.79
E2EVarNet&L+	41.0944±2.9040	38.1725±2.8973	0.9634±0.0589	0.9443±0.0698	296.30

FLOPs of different networks: enlarging the original networks or shrinking the collaboration-based networks. To apply to the VS-Net, we replace the N_s in our Network to VS-Net cascades, and we remark this method as 'VS&L+'. We also increase the cascade number in VS-Net from 10 to 15, which is remarked as 'VS-Net+'. We tested on the coronal PD sequence, and as shown in the table, improvements can be observed in 4× and 6× accelerations. We also shrink the designed network for comparison with the original VS-Net, where the number of channels in the convolutional layers was reduced to 32 from 64. The method is remarked as 'VS&L' in the table, which also outperforms the original VS-Net.

Similarly, the proposed method improved the performance of E2EVarNet. When enlarging the original E2EVarNet, we increased the number of cascades from 12 to 14 and the number of channels in the first layer from 18 to 22. To shrink the designed network, we decreased the number of channels from 16 to 8. We observe similar improvements when applying our methods to E2EVarNet. In addition, we plotted the PSNR and SSIM results of E2EVarNet-based methods at different epochs in Fig. 6. The figure clearly shows that our method (the green lines) accelerates the network convergence and improves the performance.

4.6. Subnetworks based on the same priors

The aforementioned methods adopt subnetworks based on different priors. However, model-driven methods relax the constraints of conventional algorithms. In other words, prior knowledge in model-driven networks is leveraged to form the network structure, while the networks have better flexibility to directly learn from the data compared with conventional methods.

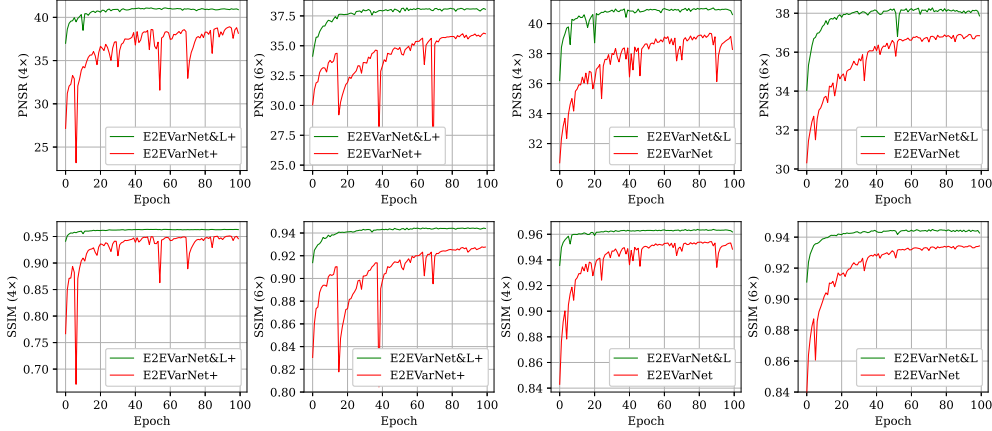


Figure 6: PSNR and SSIM results of E2EVarNet-based networks at 4-fold and 6-fold acceleration.

Table 8: Results of applying our method to other model-driven networks which based on the same prior.

structure	Method	PSNR		SSIM		FLOPs(G)
		4×	6×	4×	6×	
original	ISTA-Net	39.2910±2.8423	35.5220±3.0915	0.9471±0.0567	0.9138±0.0717	120.13
	VS-Net	40.1649±2.8767	37.0604±2.7927	0.9591±0.0569	0.9358±0.0648	265.89
	E2E-VarNet	39.3592±2.9368	36.8949±3.3872	0.9542±0.0662	0.9342±0.0775	187.87
collaboration	ISTA&VS	41.0474±3.0696	38.2371±3.1668	0.9633±0.0628	0.9440±0.0755	208.93
	VAR&VS	40.9856±3.0249	38.1867±2.9568	0.9630±0.0623	0.9438±0.0717	263.61
	ISTA&VAR	39.9858±3.1043	37.2860±2.8048	0.9594±0.0604	0.9386±0.0674	208.93
	VS(18)&VS(18)	40.9610±4.3922	37.9671±3.9082	0.9629±0.0681	0.9431±0.0696	329.00
	VS(18)&VS(16)	41.0824±3.1657	38.2279±3.4991	0.9631±0.0629	0.9441±0.0742	296.31

Therefore, even with subnetworks based on the same priors, our method can still extract complementary information to improve the network performance. To this end, we investigate the potential of leveraging the complementarity between subnetworks based on sparsity, and the results are shown in Table 8. For example, the 'ISTA&VAR' method denotes that we adopt the ISTA-Net and E2EVarNet as two subnetworks in CMD-Net. We can observe that although the final results of the networks are affected by the power of their subnetworks, collaborative networks consistently outperformed the original networks. Furthermore, we adopted the same VS-Net for both subnetworks. Specifically, we employed U-Net as the backbone in VS-Net to control its computational cost. In the 'VS(18)&VS(18)' method, the numbers of channels in the U-Net are both set to 18, 36, 72, and 144. In the

'VS(18)&VS(16)' method, the numbers of channels in one of the branches are set to 16, 32, 64, and 128. We can observe that both collaborative VS-Nets outperform the original network. More importantly, 'VS(18)&VS(16)' exhibits superior results compared to 'VS(18)&VS(18)', despite having fewer FLOPs and training parameters. These results indicate that when both subnetworks share exactly the same structure, the complementarity between subnetworks could be weakened. Conversely, introducing differences into the subnetwork structure enables them to learn distinct information, leading to improved network results. This also enhances the versatility of our network design strategy, making it easier to apply to different methods without the constraint of strictly unrolling cascades from different prior-based algorithms. In other words, our network design strategy can also be applied to model-driven methods based on single priors, further improving their results.

5. Discussion

Collaboration is an important idea in medical image reconstruction [62, 63, 64, 65, 66]. For example, the authors in [64] proposed a dual-domain reconstruction network. A V-Net in the image domain and a K-Net in k-space formed a parallel network architecture, and their outputs were linearly fused in the image domain. However, to the best of our knowledge, few of the related methods have thoroughly explored the optimal approach to organically integrate diverse priors. The authors in [44] involved sparsity and low-rankness priors in their network. They proposed to decouple the 2D Fourier transform into two separate 1D processes, allowing them to acquire a larger dataset for training the network while significantly decreasing computational complexity. In our method, we still adopted a common 2D reconstruction process to highlight the improvements brought by the proposed modules. More importantly, their network was formed with linearly stacked cascades, which alternately incorporated sparsity- and low-rankness-based regularizers to solve (31). It is quite common to incorporate different priors into the objective function in MRI reconstruction and some related fields [67, 38, 51, 68]. Conversely, we placed different regularizers based on different priors into two objective functions (i.e., (7) and (10)). Hence, two subnetworks were built. Our experimental results have shown that with the proposed attention and correction modules, our network design strategy to build multi-prior-based networks can stably achieve faster convergence and better results.

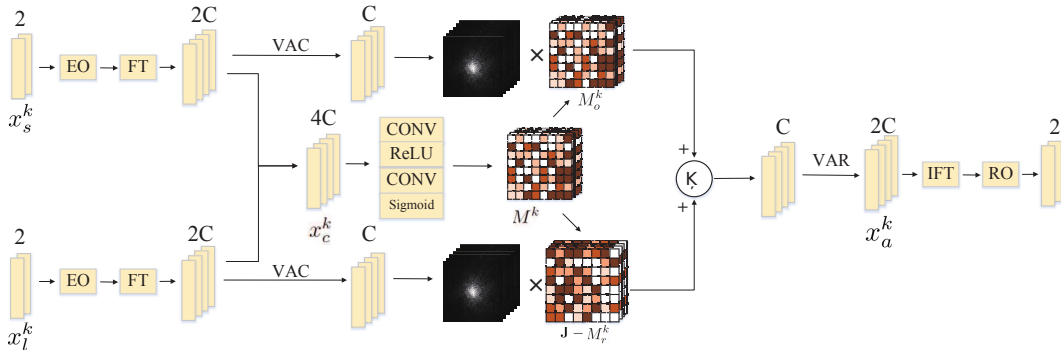


Figure 7: An attention module works in k-space.

In this study, we demonstrated that the attention-based module is highly important for integrating the intermediate results from different subnetworks. Attention mechanism has been widely applied in related reconstruction networks. For example, HUANG [14] *et al.* introduced a variant of U-net with Channel-wise Attention (UCA) module to suppress irrelevant features. In [69], the purpose of attention modules was to adaptively capture local contextual cues. The authors in [64] applied the squeeze-and-excitation (SE) attention to adaptively weight the channels. Besides, attention modules have been introduced into GANs [70, 71, 72] as indispensable components. In [73], the authors captured the long-range spatial dependencies in the frequency domain by combining self-attention with Fourier transform. However, few of them have explored to leverage the complementarity between prior knowledge using element-wise attention, and the experimental results show the obvious improvements brought by the proposed attention-based RC and OC maps.

The AMs and CMs in our network operate in the image domain. However, since MR data is acquired in k-space, directly operating in k-space could potentially lead to better accuracy. Besides, the redundancy among coil data can inherently provide rich information to build the confidence maps, thereby the method is really compatible with our network. Therefore, here we propose a simple way to extend the AMs to leverage the cross-domain information, as shown in Fig 7. We designed an enhanced CMD-Net that the AMs alternatively work in the image and frequency domains, and we observe further improvements on the results. Moreover, the proposed collaborative strategy can also be utilized to exploit the complementarity between

the cross-domain AMs. This can be explored in future works with larger datasets since handling multi-coil k-space data requires a network with more parameters.

6. Conclusion

In this study, we designed a collaborative model-driven network for MRI reconstruction. We designed RC and OC map-based attention and correction modules to maximize the contributions of different prior knowledge in their areas of expertise. Experimental results on various datasets demonstrated the superiority of our methods. When applied to other model-driven methods, clear improvements were observed without additional computational costs.

7. Acknowledgements

This work was supported by the National Natural Science Foundation of China [Nos. 62331008, 62027827, 62221005 and 62276040], National Science Foundation of Chongqing [Nos. 2023NSCQ-LZX0045 and CSTB2022NSCQ-MSX0436], Chongqing University of Posts and Telecommunications ph.D. Innovative Talents Project [BYJS202211].

References

- [1] M. G. Harisinghani, A. O’Shea, R. Weissleder, Advances in clinical mri technology, *Science Translational Medicine* 11 (2019) eaba2591.
- [2] D. Larkman, R. Nunes, Parallel magnetic resonance imaging, *Phys Med Biol* 52 (2007) R15.
- [3] D. L. Donoho, Compressed sensing, *IEEE Transactions on information theory* 52 (2006) 1289–1306.
- [4] W. Wu, D. Hu, K. An, S. Wang, F. Luo, A high-quality photon-counting ct technique based on weight adaptive total-variation and image-spectral tensor factorization for small animals imaging, *IEEE Transactions on Instrumentation and Measurement* 70 (2020) 1–14.
- [5] K. Pruessmann, M. Weiger, M. Scheidegger, P. Boesiger, Sense: sensitivity encoding for fast mri, *Magn Reson Med* 42 (1999) 952–962.

- [6] M. A. Griswold, P. M. Jakob, R. M. Heidemann, M. Nittka, V. Jellus, J. Wang, B. Kiefer, A. Haase, Generalized autocalibrating partially parallel acquisitions (grappa), *Magnetic Resonance in Medicine: An Official Journal of the International Society for Magnetic Resonance in Medicine* 47 (2002) 1202–1210.
- [7] M. Lustig, D. Donoho, J. M. Pauly, Sparse mri: The application of compressed sensing for rapid mr imaging, *Magnetic Resonance in Medicine: An Official Journal of the International Society for Magnetic Resonance in Medicine* 58 (2007) 1182–1195.
- [8] M. Lustig, D. L. Donoho, J. M. Santos, J. M. Pauly, Compressed sensing mri, *IEEE signal processing magazine* 25 (2008) 72–82.
- [9] K. Hollingsworth, Reducing acquisition time in clinical mri by data undersampling and compressed sensing reconstruction, *Phys Med Biol* 60 (2015) R297.
- [10] X. Qu, W. Zhang, D. Guo, C. Cai, S. Cai, Z. Chen, Iterative thresholding compressed sensing mri based on contourlet transform, *Inverse Probl Sci En* 18 (2010) 737–758.
- [11] S. Wang, T. Xiao, Q. Liu, H. Zheng, Deep learning for fast mr imaging: A review for learning reconstruction from incomplete k-space data, *Biomedical Signal Processing and Control* 68 (2021) 102579.
- [12] G. Yang, S. Yu, H. Dong, G. Slabaugh, P. L. Dragotti, X. Ye, F. Liu, S. Arridge, J. Keegan, Y. Guo, et al., Dagan: Deep de-aliasing generative adversarial networks for fast compressed sensing mri reconstruction, *IEEE transactions on medical imaging* 37 (2017) 1310–1321.
- [13] S. Wang, H. Cheng, L. Ying, T. Xiao, Z. Ke, H. Zheng, D. Liang, Deepcomplexmri: Exploiting deep residual network for fast parallel mr imaging with complex convolution, *Magnetic Resonance Imaging* 68 (2020) 136–147.
- [14] Q. Huang, D. Yang, P. Wu, H. Qu, J. Yi, D. Metaxas, Mri reconstruction via cascaded channel-wise attention network, in: *2019 IEEE 16th International Symposium on Biomedical Imaging (ISBI 2019)*, IEEE, 2019, pp. 1622–1626.

- [15] M. Akçakaya, S. Moeller, S. Weingärtner, K. Uğurbil, Scan-specific robust artificial-neural-networks for k-space interpolation (raki) reconstruction: Database-free deep learning for fast imaging, *Magnetic resonance in medicine* 81 (2019) 439–453.
- [16] M. Mardani, E. Gong, J. Y. Cheng, S. S. Vasanawala, G. Zaharchuk, L. Xing, J. M. Pauly, Deep generative adversarial neural networks for compressive sensing mri, *IEEE transactions on medical imaging* 38 (2018) 167–179.
- [17] T. M. Quan, T. Nguyen-Duc, W.-K. Jeong, Compressed sensing mri reconstruction using a generative adversarial network with a cyclic loss, *IEEE transactions on medical imaging* 37 (2018) 1488–1497.
- [18] R. Noor, A. Wahid, S. U. Bazai, A. Khan, M. Fang, M. Syam, U. A. Bhatti, Y. Y. Ghadi, Dlgan: Undersampled mri reconstruction using deep learning based generative adversarial network, *Biomedical Signal Processing and Control* 93 (2024) 106218.
- [19] D. Hu, Y. Zhang, J. Zhu, Q. Liu, Y. Chen, Trans-net: Transformer-enhanced residual-error alternative suppression network for mri reconstruction, *IEEE Transactions on Instrumentation and Measurement* 71 (2022) 1–13.
- [20] J. Zhang, B. Ghanem, Ista-net: Interpretable optimization-inspired deep network for image compressive sensing, in: *Proceedings of the IEEE conference on computer vision and pattern recognition*, 2018, pp. 1828–1837.
- [21] J. Duan, J. Schlemper, C. Qin, C. Ouyang, W. Bai, C. Biffi, G. Bello, B. Statton, D. P. O’regan, D. Rueckert, Vs-net: Variable splitting network for accelerated parallel mri reconstruction, in: *Medical Image Computing and Computer Assisted Intervention–MICCAI 2019: 22nd International Conference, Shenzhen, China, October 13–17, 2019, Proceedings, Part IV* 22, Springer, 2019, pp. 713–722.
- [22] A. Sriram, J. Zbontar, T. Murrell, A. Defazio, C. L. Zitnick, N. Yakubova, F. Knoll, P. Johnson, End-to-end variational networks for

- accelerated mri reconstruction, in: *Medical Image Computing and Computer Assisted Intervention–MICCAI 2020: 23rd International Conference, Lima, Peru, October 4–8, 2020, Proceedings, Part II* 23, Springer, 2020, pp. 64–73.
- [23] K. Hammernik, T. Klatzer, E. Kobler, M. P. Recht, D. K. Sodickson, T. Pock, F. Knoll, Learning a variational network for reconstruction of accelerated mri data, *Magnetic resonance in medicine* 79 (2018) 3055–3071.
- [24] G. Yiasemis, J.-J. Sonke, C. Sánchez, J. Teuwen, Recurrent variational network: a deep learning inverse problem solver applied to the task of accelerated mri reconstruction, in: *Proceedings of the IEEE/CVF Conference on Computer Vision and Pattern Recognition, 2022*, pp. 732–741.
- [25] E. Z. Chen, P. Wang, X. Chen, T. Chen, S. Sun, Pyramid convolutional rnn for mri image reconstruction, *IEEE Transactions on Medical Imaging* 41 (2022) 2033–2047.
- [26] Z. Ramzi, G. Chaithya, J.-L. Starck, P. Ciuciu, Nc-pdnet: A density-compensated unrolled network for 2d and 3d non-cartesian mri reconstruction, *IEEE Transactions on Medical Imaging* 41 (2022) 1625–1638.
- [27] H. K. Aggarwal, M. P. Mani, M. Jacob, Modl: Model-based deep learning architecture for inverse problems, *IEEE transactions on medical imaging* 38 (2018) 394–405.
- [28] Y. Jun, H. Shin, T. Eo, D. Hwang, Joint deep model-based mr image and coil sensitivity reconstruction network (joint-icnet) for fast mri, in: *Proceedings of the IEEE/CVF Conference on Computer Vision and Pattern Recognition, 2021*, pp. 5270–5279.
- [29] T. Lu, X. Zhang, Y. Huang, D. Guo, F. Huang, Q. Xu, Y. Hu, L. Ouyang, J. Lin, Z. Yan, et al., pfista-sense-resnet for parallel mri reconstruction, *Journal of Magnetic Resonance* 318 (2020) 106790.
- [30] J. Sun, H. Li, Z. Xu, et al., Deep admm-net for compressive sensing mri, *Advances in neural information processing systems* 29 (2016).

- [31] D. Zhao, Y. Huang, Y. Gan, J. Zheng, J-loucr: Joint learned optimized undersampling and constrained reconstruction for accelerated mri by reference-driven deep image prior, *Biomedical Signal Processing and Control* 87 (2024) 105513.
- [32] A. Beck, M. Teboulle, A fast iterative shrinkage-thresholding algorithm for linear inverse problems, *SIAM journal on imaging sciences* 2 (2009) 183–202.
- [33] G. Yiasemis, N. Moriakov, J.-J. Sonke, J. Teuwen, vsharp: variable splitting half-quadratic admm algorithm for reconstruction of inverse-problems, *arXiv preprint arXiv:2309.09954* (2023).
- [34] Y. Yang, J. Jia, An image reconstruction algorithm for electrical impedance tomography using adaptive group sparsity constraint, *IEEE Transactions on Instrumentation and Measurement* 66 (2017) 2295–2305.
- [35] S. Wang, H. Yu, Y. Xi, C. Gong, W. Wu, F. Liu, Spectral-image decomposition with energy-fusion sensing for spectral ct reconstruction, *IEEE Transactions on Instrumentation and Measurement* 70 (2021) 1–11.
- [36] J. Ye, H. Wang, W. Yang, Image recovery for electrical capacitance tomography based on low-rank decomposition, *IEEE Transactions on Instrumentation and Measurement* 66 (2017) 1751–1759.
- [37] T. Qiu, W. Liao, Y. Huang, J. Wu, D. Guo, D. Liu, X. Wang, J.-F. Cai, B. Hu, X. Qu, An automatic denoising method for nmr spectroscopy based on low-rank hankel model, *IEEE Transactions on Instrumentation and Measurement* 70 (2021) 1–12.
- [38] Z. Ke, W. Huang, Z.-X. Cui, J. Cheng, S. Jia, H. Wang, X. Liu, H. Zheng, L. Ying, Y. Zhu, et al., Learned low-rank priors in dynamic mr imaging, *IEEE Transactions on Medical Imaging* 40 (2021) 3698–3710.
- [39] X. Zhang, D. Guo, Y. Huang, Y. Chen, L. Wang, F. Huang, Q. Xu, X. Qu, Image reconstruction with low-rankness and self-consistency of k-space data in parallel mri, *Medical Image Analysis* 63 (2020) 101687.

- [40] K. H. Jin, D. Lee, J. C. Ye, A general framework for compressed sensing and parallel mri using annihilating filter based low-rank hankel matrix, *IEEE Transactions on Computational Imaging* 2 (2016) 480–495.
- [41] M. Jacob, M. P. Mani, J. C. Ye, Structured low-rank algorithms: Theory, magnetic resonance applications, and links to machine learning, *IEEE signal processing magazine* 37 (2020) 54–68.
- [42] A. Pramanik, H. K. Aggarwal, M. Jacob, Deep generalization of structured low-rank algorithms (deep-slr), *IEEE transactions on medical imaging* 39 (2020) 4186–4197.
- [43] X. Zhang, H. Lu, D. Guo, Z. Lai, H. Ye, X. Peng, B. Zhao, X. Qu, Accelerated mri reconstruction with separable and enhanced low-rank hankel regularization, *IEEE Transactions on Medical Imaging* 41 (2022) 2486–2498.
- [44] Z. Wang, C. Qian, D. Guo, H. Sun, R. Li, B. Zhao, X. Qu, One-dimensional deep low-rank and sparse network for accelerated mri, *IEEE Transactions on Medical Imaging* 42 (2022) 79–90.
- [45] X. Qu, M. Mayzel, J.-F. Cai, Z. Chen, V. Orekhov, Accelerated nmr spectroscopy with low-rank reconstruction, *Angewandte Chemie International Edition* 54 (2015) 852–854.
- [46] Y. Huang, J. Zhao, Z. Wang, V. Orekhov, D. Guo, X. Qu, Exponential signal reconstruction with deep hankel matrix factorization, *IEEE Transactions on Neural Networks and Learning Systems* (2021).
- [47] N. Srebro, Learning with matrix factorizations, massachusetts institute of technology (2004).
- [48] S. Boyd, N. Parikh, E. Chu, B. Peleato, J. Eckstein, et al., Distributed optimization and statistical learning via the alternating direction method of multipliers, *Foundations and Trends® in Machine learning* 3 (2011) 1–122.
- [49] S. G. Lingala, Y. Hu, E. DiBella, M. Jacob, Accelerated dynamic mri exploiting sparsity and low-rank structure: kt slr, *IEEE transactions on medical imaging* 30 (2011) 1042–1054.

- [50] R. Otazo, E. Candes, D. K. Sodickson, Low-rank plus sparse matrix decomposition for accelerated dynamic mri with separation of background and dynamic components, *Magnetic resonance in medicine* 73 (2015) 1125–1136.
- [51] C. Y. Lin, J. A. Fessler, Efficient dynamic parallel mri reconstruction for the low-rank plus sparse model, *IEEE transactions on computational imaging* 5 (2018) 17–26.
- [52] A. Majumdar, R. K. Ward, T. Aboulnasr, Non-convex algorithm for sparse and low-rank recovery: Application to dynamic mri reconstruction, *Magnetic resonance imaging* 31 (2013) 448–455.
- [53] M. Arvinte, S. Vishwanath, A. H. Tewfik, J. I. Tamir, Deep j-sense: Accelerated mri reconstruction via unrolled alternating optimization, in: *International conference on medical image computing and computer-assisted intervention*, Springer, 2021, pp. 350–360.
- [54] K. Mohan, M. Fazel, Iterative reweighted algorithms for matrix rank minimization, *The Journal of Machine Learning Research* 13 (2012) 3441–3473.
- [55] Y. Liu, Z. Zhan, J.-F. Cai, D. Guo, Z. Chen, X. Qu, Projected iterative soft-thresholding algorithm for tight frames in compressed sensing magnetic resonance imaging, *IEEE transactions on medical imaging* 35 (2016) 2130–2140.
- [56] X. Zhang, H. Lu, D. Guo, L. Bao, F. Huang, Q. Xu, X. Qu, A guaranteed convergence analysis for the projected fast iterative soft-thresholding algorithm in parallel mri, *Medical Image Analysis* 69 (2021) 101987.
- [57] J. Zbontar, F. Knoll, A. Sriram, T. Murrell, Z. Huang, M. J. Muckley, A. Defazio, R. Stern, P. Johnson, M. Bruno, et al., fastmri: An open dataset and benchmarks for accelerated mri, *arXiv preprint arXiv:1811.08839* (2018).
- [58] M. Uecker, P. Lai, M. J. Murphy, P. Virtue, M. Elad, J. M. Pauly, S. S. Vasanawala, M. Lustig, Espirit—an eigenvalue approach to autocalibrating parallel mri: where sense meets grappa, *Magnetic resonance in medicine* 71 (2014) 990–1001.

- [59] F. Ong, M. Lustig, Sigpy: a python package for high performance iterative reconstruction, in: Proceedings of the ISMRM 27th Annual Meeting, Montreal, Quebec, Canada, volume 4819, 2019.
- [60] S. Ma, W. Yin, Y. Zhang, A. Chakraborty, An efficient algorithm for compressed mr imaging using total variation and wavelets, in: 2008 IEEE Conference on Computer Vision and Pattern Recognition, IEEE, 2008, pp. 1–8.
- [61] J. Schlemper, J. Caballero, J. V. Hajnal, A. Price, D. Rueckert, A deep cascade of convolutional neural networks for mr image reconstruction, in: Information Processing in Medical Imaging: 25th International Conference, IPMI 2017, Boone, NC, USA, June 25-30, 2017, Proceedings 25, Springer, 2017, pp. 647–658.
- [62] C. Wang, K. Shang, H. Zhang, Q. Li, Y. Hui, S. K. Zhou, Dudotrans: dual-domain transformer provides more attention for sinogram restoration in sparse-view ct reconstruction, arXiv preprint arXiv:2111.10790 (2021).
- [63] R. Ge, Y. He, C. Xia, H. Sun, Y. Zhang, D. Hu, S. Chen, Y. Chen, S. Li, D. Zhang, Ddpnet: A novel dual-domain parallel network for low-dose ct reconstruction, in: International Conference on Medical Image Computing and Computer-Assisted Intervention, Springer, 2022, pp. 748–757.
- [64] X. Liu, Y. Pang, R. Jin, Y. Liu, Z. Wang, Dual-domain reconstruction network with v-net and k-net for fast mri, Magnetic Resonance in Medicine 88 (2022) 2694–2708.
- [65] T. Eo, Y. Jun, T. Kim, J. Jang, H.-J. Lee, D. Hwang, Kiki-net: cross-domain convolutional neural networks for reconstructing undersampled magnetic resonance images, Magnetic resonance in medicine 80 (2018) 2188–2201.
- [66] Z. Tu, C. Jiang, Y. Guan, J. Liu, Q. Liu, K-space and image domain collaborative energy-based model for parallel mri reconstruction, Magnetic Resonance Imaging 99 (2023) 110–122.

- [67] O. Mokry, J. Vitouš, P. Rajmic, R. Jiřík, Improving dce-mri through unfolded low-rank+ sparse optimisation, arXiv preprint arXiv:2312.07222 (2023).
- [68] W. Huang, Z. Ke, Z.-X. Cui, J. Cheng, Z. Qiu, S. Jia, L. Ying, Y. Zhu, D. Liang, Deep low-rank plus sparse network for dynamic mr imaging, *Medical Image Analysis* 73 (2021) 102190.
- [69] J. Liu, C. Qin, M. Yaghoobi, Coil-agnostic attention-based network for parallel mri reconstruction, in: *Proceedings of the Asian Conference on Computer Vision, 2022*, pp. 2866–2883.
- [70] Z. Yuan, M. Jiang, Y. Wang, B. Wei, Y. Li, P. Wang, W. Menpes-Smith, Z. Niu, G. Yang, Sara-gan: Self-attention and relative average discriminator based generative adversarial networks for fast compressed sensing mri reconstruction, *Frontiers in Neuroinformatics* 14 (2020) 611666.
- [71] Y. Wu, Y. Ma, J. Liu, J. Du, L. Xing, Self-attention convolutional neural network for improved mr image reconstruction, *Information sciences* 490 (2019) 317–328.
- [72] W. Zhou, H. Du, W. Mei, L. Fang, Spatial orthogonal attention generative adversarial network for mri reconstruction, *Medical Physics* 48 (2021) 627–639.
- [73] L. Zhou, M. Zhu, D. Xiong, L. Ouyang, Y. Ouyang, Z. Chen, X. Zhang, Rnlfnet: Residual non-local fourier network for undersampled mri reconstruction, *Biomedical Signal Processing and Control* 83 (2023) 104632.